Nuclear Science Experiments with a Bright Neutron Source from Fusion Reactions on the OMEGA Laser System

Introduction

Inertial confinement fusion (ICF) experiments are designed to study the hydrodynamic nature of high-energy-density plasmas to achieve ignition and gain in laboratory experiments.[1] In direct-drive ICF experiments on LLE's OMEGA Laser System,[2] neutrons are produced using a laser to implode microballoons filled with deuterium–tritium (DT) fuel.[3] The dominant fusion reaction in these implosions is

$$\mathrm{D} + \mathrm{T} \rightarrow {}^{4}\mathrm{He}(3.52\ \mathrm{MeV}) + \mathrm{n}(14.03\ \mathrm{MeV}). \quad (1)$$

Two additional primary fusion reactions, D + D and T + T (Ref. 4), make a much smaller contribution ($\sim 10^{-2}$) compared to the overall yield and have a negligible impact on the experimental measurements presented in this article. One particular class of implosions—"exploding pushers"[5]—uses thin glass shells that can produce neutron yields in excess of 1×10^{14} with pulse durations of the order of $\approx$1 ns and energy on target of ~30 kJ (Ref. 6).

To test a modern microscopic nuclear theory, an experiment to measure the neutron-induced breakup of light nuclei has been developed. This platform could prove to be a valuable tool for nuclear physicists since experimental data are scarce and incomplete; in particular, for energy spectra of neutrons from D(n,2n)p breakup occurring in a thermonuclear ICF environment. The present quality of the measured breakup energy spectrum from deuterium does not permit a clear conclusion with respect to recent theoretical models that have been proposed.[7] For this reason, the breakup of deuterons is a good candidate to demonstrate the capability of this experimental platform.

The reaction being studied in this experiment is expressed as

$$\mathrm{n}(14\ \mathrm{MeV}) + \mathrm{D} \rightarrow 2\mathrm{n}(0 - 11.8\ \mathrm{MeV}) + \mathrm{p}(0 - 11.8\ \mathrm{MeV}). \quad (2)$$

Here the energy ranges of the reaction products are given in parentheses.[8]

An experimental setup was developed on the OMEGA Laser System to use these monoenergetic neutron sources to investigate the breakup of light nuclei. The experimental platform consists of a subnanosecond, high-yield 14-MeV neutron pulse incident on a reaction vessel filled with the target compound. A reaction vessel filled with deuterated compounds is located as close as possible to the implosion, maximizing the solid angle without interfering with the laser pulses required for illuminating the microballoon.

The spectra from primary fusion reactions and the breakup of the light nuclei are recorded with a high-dynamic-range, high-resolution neutron time-of-flight (nTOF) spectrometer. This diagnostic is located in a highly collimated line of sight and filled with a low-afterglow liquid scintillator contained inside a thin steel housing positioned in-line with the reaction vessel.[9] It was designed to have a dynamic range of up to 10^6 with the capability to measure the neutron energy spectrum over an energy range of 0.5 MeV to 15 MeV. A schematic of the experimental setup is shown in Fig. 153.1.

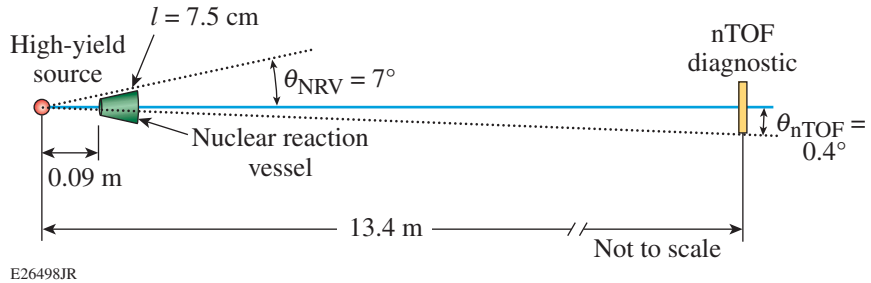

Figure 153.1
The experimental setup consists of a high-yield neutron source incident on a nuclear reaction vessel (NRV). The vessel contains either non-deuterated or deuterated compounds necessary for direct comparison with the neutron-induced breakup reaction. The neutron signal is measured using a high-dynamic-range, high-resolution time-of-flight diagnostic positioned 13.4 m from the target chamber center. Signals are sent to a diagnostic rack and digitized for analysis. nTOF: neutron time of flight.

This article presents for the first time an experimental setup for which a laser-based facility has been used to measure the neutron-induced breakup reactions of light nuclei. The following sections (1) provide details about the experimental setup and configuration to induce the breakup reactions along with the diagnostic used to measure the nTOF spectra; (2) present details on the calibration of the diagnostic, essential for calculating the neutron energy spectrum from the breakup yield; (3) discuss the experimental data along with the uncertainty in the measurements; and (4) summarize our findings and discuss future experiments.

Experimental Setup and Configuration

1. High-Yield Neutron Source

The bright neutron source (14 MeV) generated for this experiment uses an exploding-pusher design with a thin-walled (~3-μm), ~1-mm-diam SiO_2 microballoon filled with 10 atm of equimolar DT fuel.[10,11] The laser beams deliver up to 30 kJ of energy onto the target with a nominal 1-ns square pulse. The symmetric illumination with the 60 UV laser beams rapidly heats the thin shell, expands, and drives a shock wave into the fuel.[12] This shock wave compresses and heats the fuel as it converges at the center of the target. As the shock rebounds, the fuel reaches sufficient temperatures to produce thermonuclear fusion reactions, with neutron yields of up to 1×10^{14} emitted in 4π. In this implosion design, the bang time (time when peak neutron production takes place) is ~1 ns after the laser is incident on the target with a neutron-production width of ~100 ps (Ref. 13). The neutron-emitting region (hot spot) for this class of implosions is ~100 μm in diameter. An example of the laser pulse along with the neutron temporal emission history is shown in Fig. 153.2.

2. Nuclear Reaction Vessel

The nuclear reaction vessel (NRV) in constructed from thin (1-mm) aluminum to minimize additional neutron scattering. Figure 153.3(a) shows a photograph of the reaction vessel attached to the support bracket; Fig. 153.3(b) shows a close-up of the vessel. A pointer was designed to mount in place of the reaction vessel to allow one to align the system. The overall length of the truncated cone-shaped vessel is 7.5 cm with the smallest diameter being 0.9 cm and the largest diameter being 4 cm. The vessel was specially designed to be positioned 9 cm from the center of the OMEGA target chamber to ensure that the incoming laser beams have a clear path to illuminate the microballoon. The vessels are attached to a specially designed bracket mounted in one of the ten-inch manipulator (TIM) diagnostic ports on the target chamber. As with the vessel requirements, the bracket was designed with minimal mass in order to avoid additional neutron scattering along the detector's line of sight. Because of the geometry of the vessel with respect

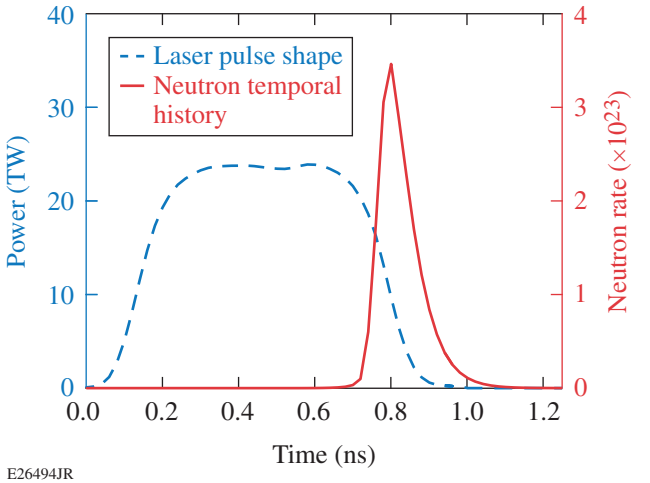

Figure 153.2
A plot showing the nominal 1-ns square laser pulse and neutron production rate from a typical exploding pusher on OMEGA. Peak neutron production (bang time) takes place ~800 ps from the moment light is incident on the target. The burnwidth for this class of implosions is of the order of a 100-ps full width at half maximum (FWHM).

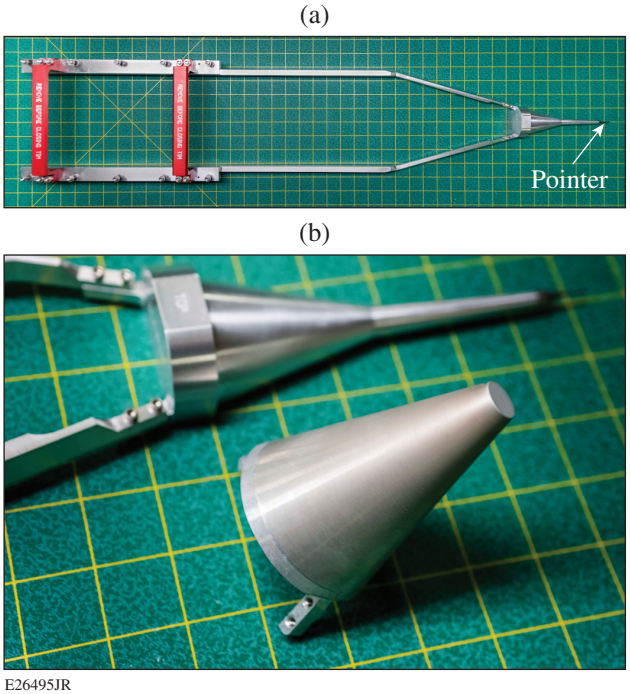

Figure 153.3
(a) A support frame designed to be mounted in one of the diagnostic ports on the OMEGA target chamber. (b) The nuclear reaction vessel is constructed from thin aluminum to minimize additional neutron scattering. The face of the vessel is positioned 9 cm from the high-yield neutron source.

to the diagnostic, this measurement will cover an angle normal to the vessel of $\theta_{lab} = 3.5° \pm 3.5°$.

3. Highly Collimated Line of Sight

High-yield DT implosions on OMEGA generate an unwanted background signal from neutron scattering in the target chamber walls and surrounding concrete structures inside the Target Bay, such as the OMEGA end-mirror structures. For this reason, the primary diagnostic is positioned in a shielded, highly collimated line of sight to increase the signal-to-background ratio of the measurements.[14] The detector is mounted in a low-scattering environment underneath the Target Bay floor, 13.4 m from the target chamber center (TCC). A 21-cm-diam hole in the 60-cm-thick concrete floor acts as a collimator close to the time-of-flight diagnostic. A mid-beam collimator was designed to be the defining aperture of the neutron beam to reduce the detector's field of view from the target chamber. The mid-beam collimator has a 60-cm^2 cross section and is ~70 cm in length. It is constructed from high-density polyethylene (~0.95 g/cm^3) and mounted on a semi-permanent stand located inside the OMEGA Target Bay and positioned approximately halfway between TCC and a concrete barrier as shown in Fig. 153.4.

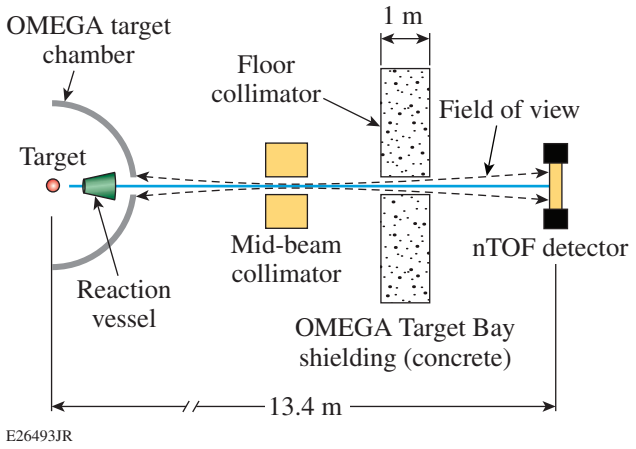

Figure 153.4
The 13.4-m nTOF is positioned in a clear line of sight through the TIM-6 diagnostic port (not shown). A thick concrete floor acts as collimator to shield the diagnostic from unwanted neutron scattering off the surrounding structure in the Target Bay. A mid-beam collimator is mounted between the target chamber and the diagnostic. TIM: ten-inch manipulator.

4. Liquid-Scintillator Detector

The diagnostic used to measure the neutron energy spectrum in this study is a four-microchannel-plate photomultiplier tube (MCP-PMT) detector design positioned 13.4 m from TCC.[15] It consists of a 20-cm-diam, 10-cm-deep stainless-steel cylindrical housing that contains the scintillation fluid. This detector uses a thin-walled (2-mm) construction to minimize neutron scattering within the scintillator housing. Thin (<0.3-cm) stainless-steel end plates are used to seal the cylindrical housing to minimize neutron attenuation. The ports for the MCP-PMT are 40-mm-diam fused-silica windows mounted on the cylindrical housing and sealed with Viton O rings. This diagnostic uses oxygenated xylene doped with *diphenyloxazole* $C_{15}H_{11}NO$ + *p*-bis-(o-methylstyryl)-benzene (PPO + bis-MSB) wavelength-shifting dyes, which generates light emission in the visible to near-ultraviolet wavelength range (i.e., from 380 μm to 420 μm). This oxygenated liquid scintillator has a fast time response with a low-light afterglow.[16] A computer-aided drawing of the nTOF diagnostic with the MCP-PMT's is shown in Fig. 153.5.

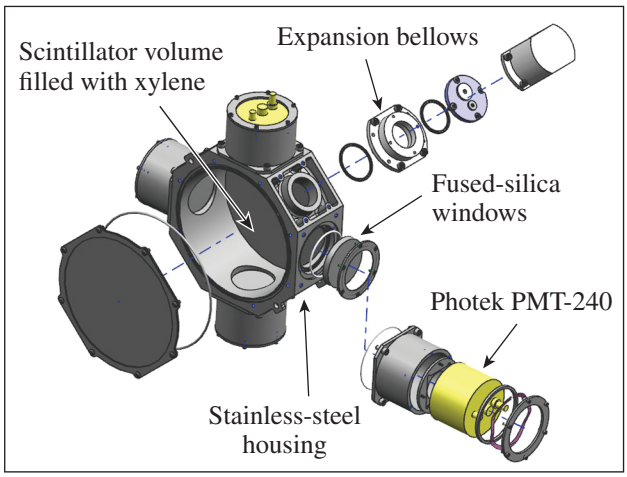

Figure 153.5
A CAD drawing of the nTOF detector shows a cavity for the scintillation fluid, the fused-silica windows, and the photomultiplier-tube (PMT) mounts. The detector is mounted in a shielded environment behind a concrete barrier to minimize unwanted neutron scattering.

5. Gated Microchannel-Plate Detectors

The light emitted by the scintillator process is viewed through fused-silica windows, where it is coupled to four Photek 40-mm-diam MCP-PMT's.[17] These PMT's are designed to operate in current mode in order to measure the significant photon flux generated from up to 1×10^7 incident neutrons interacting in the scintillation volume. Each of the four PMT's is operated at a different high voltage that corresponds to the desired gain (see Table 153.I) required for measuring the nTOF signal and to achieve a dynamic range in yield of up to 10^6. To ensure that measurements are not compromised because of charge depletion of the MCP, off-line tests were performed

Table 153.I: Nominal MCP-PMT high-voltage and gate-timing setup for the 13.4-m neutron time-of-flight diagnostic.

PMT assignment	MCP-PMT	High voltage (V)	Gain	Gate timing (ns)
A	Photek-140	3875	10	N/A
B	Photek-240	4500	10,000	1090
C	Photek-140	4150	200	730
D	Photek-240	4350	400	815

MCP: microchannel plate; PMT: photomultiplier tube.

on each of the MCP-PMT's at the specified gain to confirm that signal linearity is preserved. Fast-gating units allow the MCP-PMT unit to turn off and on with a recovery time of ~30 ns. The gate-timing windows are predetermined to record a particular region of interest in the time-of-flight spectrum, excluding the PMT-A, which remains ungated to measure the primary DT peak. The gate-timing signals are generated using an SRS DG-635 digital pulse generator[18] that is timed from the OMEGA Hardware Timing System (HTS).

6. Signal Transport and Data Acquisition

The analog signals from the MCP-PMT's are transmitted to the oscilloscope using ~5-m-long LMR-600 cables.[19] Three of the MCP-PMT's signals are sent to eight-bit, 1-GHz Tektronix DPO 7104 digital oscilloscopes, while the fourth MCP-PMT signal is sent to a 12-bit, 250-MHz LeCroy HDO6104-MS digital oscilloscope.[20,21] The signal from each PMT is spilt into separate oscilloscope channels using three-way 1-GHz splitters.[22] The fourth channel on each of the oscilloscopes is reserved for the OMEGA timing fiducial, which is used for absolute timing of the system. For consistency, these cables were checked by analyzing the frequency-dependent loss using an Agilent Microwave Analyzer to measure the attenuation as a function of the frequency and compared to the results in the manufacturer's published specifications.[23] These tests confirmed that there is negligible attenuation in the measured signal output with the use of short cables and input signals in the frequency range <1000 MHz.

7. Beamline Attenuation

The beamline attenuation as a function of neutron energy has been modeled using a neutron transport code (MCNP) to obtain the fraction of the neutrons that are incident on the detector relative to the source originating at TCC in different configurations. The baseline configuration includes the point neutron source and the neutron detector excluding air and the surrounding structure. A second simulation introduced air to illustrate the amount of attenuation of the neutrons as they travel toward the detector. The final simulation includes all the large-scale structures such as the target chamber (aluminum) and concrete shielding. Additional sources that could contribute to unwanted scattering in the specified line of sight include the TIM with a 1.9-mm stainless-steel vacuum window that separates the vacuum from the air, the mid-beam collimator, and the air gap (7.5 m) between the end of the TIM and the detector. The resulting beamline attenuation from the separate simulations in this line of sight is shown in Fig. 153.6 (Ref. 24). The neutron attenuation can be as high as 20% with energies below 2 MeV. It should be noted that neutron attenuation is included in the MCNP simulation, which modeled the energy spectrum of neutrons emitted from the physics target (see **D–D Yield Calibration**, below). Uncertainties in the beamline attenuation are governed by the accuracy of the experimentally measured cross sections for the material used in these simulations.[25] Detailed geometry of the model is also required to further reduce the uncertainty of the simulations and was referenced from computer-aided drawings for accuracy and completeness.

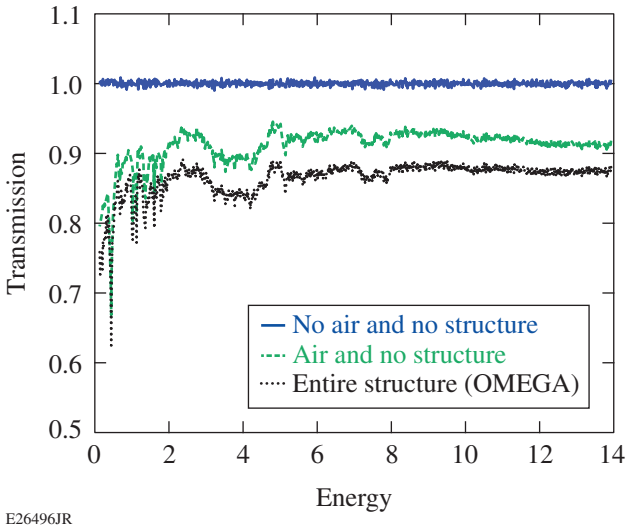

Figure 153.6
Three different simulations were performed to illustrate the attenuation in the 13.4-m beamline. The first configuration is without any air or structure in the target environment. Adding air in the line of sight emphasizes the loss of neutrons below 2 MeV in addition to the absorption regions from 2 to 4 MeV. The remaining structure in the beamline includes the stainless-steel plate that reduces the signal approximately uniformly over 1 to 14 MeV.

Detector Calibration

1. D–D Yield Calibration

The 13.4-m nTOF detector is typically calibrated using two D_2-filled target shots with different implosion parameters, producing yields that differ by a factor of ~10. The signals from

the photomultiplier tubes are measured on the oscilloscope as time-dependent currents $I(t_n)$, which can be expressed in terms of $H(t_n)$ as

$$I(t_n) = \frac{dC(t_n)}{dt_n} = \frac{1}{k_1}\frac{dH(t_n)}{dt_n}, \quad (3)$$

where $H(t_n)$ is the scintillator light output measured in MeVee (electron equivalent), C is the charge in coulombs, and k_1 = MeVee/pC is a constant. The nonlinear relation between the light output for a single neutron absorbed H_n and the neutron energy E_n can be approximated by the power law

$$H_n(t_n) = k_2 * E_n^{\alpha}(t_n), \quad (4)$$

where α is the power law coefficient, k_2 is in units of MeVee/MeV$^{\alpha}$, and E_n is the energy of the neutron as a function of arrival time t_n to the diagnostic.[26] In the literature, measurements of the proton light response for xylene-based solvents scale as $\alpha \sim 0.3$ (Refs. 27–29). Total light output as a function of time for all neutrons that deposit energy in the scintillator can be expressed by the following relation:

$$\frac{dH(t_n)}{dt_n} = k_2 E^{\alpha}\chi_n(E_n)\frac{dY(t_n)}{dE_n}\frac{dE_n}{dt_n}, \quad (5)$$

where $\chi_n(E_n)$ is defined as the fraction of neutron kinetic energy deposited in the scintillator. The relation between the measured photomultiplier current $I(t_n)$ and the scintillator light output $dH(t_n)/dt_n$ is used to infer the neutron yield Y_n measured for the time-of-flight interval $(t_n, t_n + dt_n)$ using Eq. (3):

$$dY_n(t_n) = \frac{k_1}{k_2}\frac{1}{\chi_n(E_n)E_n^{\alpha}} I(t_n)dt_n. \quad (6)$$

For a monoenergetic reaction, in the case of a D–D fusion product, Eq. (6) can be solved approximately as

$$dY_n(t_n) = \frac{k_1}{k_2}\left[\frac{1}{\chi_{D_2}E_{D_2}^{\alpha}}\right]\Bigg|_{E_{D_2}} I(t_n)dt_n, \quad (7)$$

where $1/\chi_{D_2}E_{D_2}^{\alpha}$ is a constant that allows for integration over the D_2 peak neutron distribution in time. The charge measured by each of the PMT's at the detector positioned at 13.4 m is cross-calibrated against the standard D–D neutron yield measurements on OMEGA to obtain a calibration constant k_1/k_2 for monoenergetic neutrons defined by

$$\frac{k_1}{k_2} = \frac{Y_{D_2}\chi_{D_2}E_{D_2}^{\alpha}}{I_{D_2}} \quad (8)$$

with units of MeV$^{\alpha}$/pC. The constant k_1/k_2 is required to infer the yield over all energies. It is important to note that two factors will change k_1/k_2: (1) scintillator degradation that changes the light output as a function of neutron energy and (2) the gain of the MCP-PMT, which is a nonlinear function of the high voltage.[30] The energy deposition $\chi_n(E_n)$ is calculated using MCNP to model the fraction of neutron kinetic energy deposited in the scintillator. The model consists of a 20-cm-diam, 10-cm-thick volume of liquid xylene (C_8H_{10}), with monoenergetic neutrons ranging from 0.5 to 14 MeV incident on the volume. The energy deposition in the scintillator is tallied in the simulation code. It is assumed that the neutrons in these simulations arrived at the detector at time (t) and with an energy $E_n(t_n)$ that depends on their time of flight. This is a good approximation since the probability of an outgoing neutron, with a given energy, undergoing multiple scattering interactions from surrounding support structures and still arriving at the detector is negligible.

2. Signal Timing

To relate the time-of-flight spectrum to an absolute energy spectrum, the oscilloscope is timed using semiannual dedicated shot time on OMEGA, producing ultrashort x rays (<20 ps) that are measured by the detector system and correlated to the fiducial for absolute timing. The fiducial is correlated to laser light incident on the target to within an uncertainty of ~10 ps and originates from the OMEGA HTS. The optical fiducial is sent to the oscilloscope using a fiber optic cable, where it is converted to an electrical signal using a photodiode located just before the input channel. The recorded fiducial pulse is fitted by a pulse train of eight Gaussian distributions spaced apart at the well-characterized period of Δt_f = 548 ps:

$$\text{fidu}(t) = \sum_{i=0}^{7}\frac{a_i}{\sqrt{2\pi\sigma^2}}\left\{-\left[t-\left(t_0 + i\times\Delta t_f\right)\right]^2/2\sigma^2\right\} \quad (9)$$

to the recorded signals. Here, a_i is the amplitude of each fiducial peak, t_0 is the time of the first fiducial pulse, and σ is the width of an individual pulse.

The oscilloscope is timed to within an uncertainty of 1 ns using the measured arrival time of the x-ray pulse and the well-measured distance of the diagnostic to TCC. Furthermore,

the fiducial recorded during the calibration including the x-ray pulse is used to preserve the timing for each signal recorded.

Experimental Results and Error Analysis

1. Time-of-Flight Spectra

A first set of experiments used vessels that contained deuterated compounds such as D_2O and C_6D_6 to investigate the breakup of deuterium. Additional measurements were made using vessels filled with standard non-deuterated compounds (H_2O, C_6H_6) in order to identify contributions attributed to the inelastic scattering of oxygen and carbon in the NRV from the 14-MeV neutrons. For each reaction vessel, up to six implosions with yields of $\sim 7 \times 10^{13}$ were performed for both the non-deuterated and deuterated samples. First, the primary D–T yield signal from a separate (monitor) standard diagnostic, which has an uncertainty of 5%, was used to normalize each measured breakup neutron signal to the primary yield.[31] Second, the signals that used one specific vessel were averaged to increase the signal-to-noise ratio. A comparison between the vessels filled with the deuterated and non-deuterated compounds, where the time-of-flight spectra were averaged, clearly shows the contribution from the neutron-induced breakup between the primary DT and D_2 as presented in Fig. 153.7. In both cases, there was the possibility for additional absorption and scattering effects of the neutrons generated in the breakup reaction. A brief discussion on the effects of multiple scattering within the vessel is given in **Multiple Scattering Effects** (p. 9). The measured time-of-flight signal spans up to six orders in magnitude. As previously discussed, these nTOF measurements are achieved by setting each of the four MCP-PMT's to a specific gain. The contributions for each phototube are represented by the different shaded regions. A single excited state (7.0 MeV)

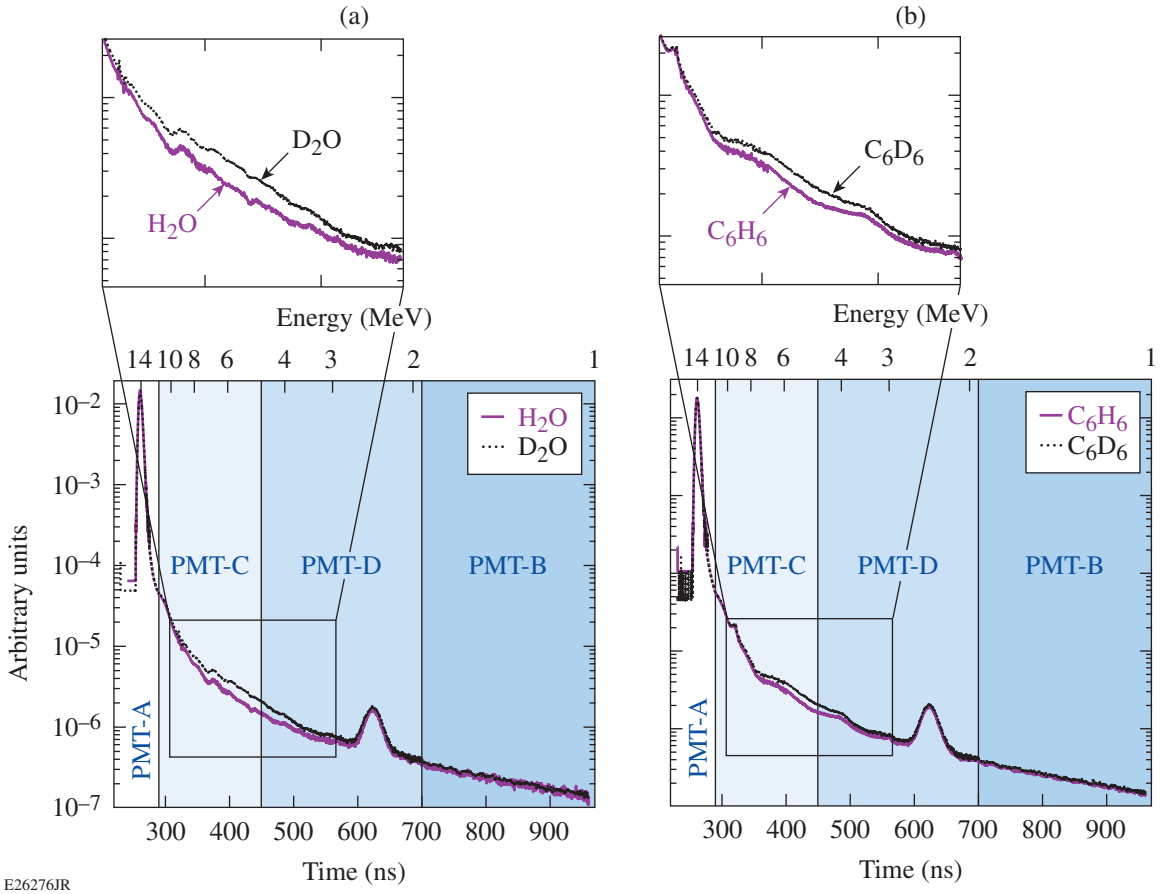

Figure 153.7

A bright neutron source was used to induce a breakup reaction in the reaction vessel filled with deuterated compounds. A comparison of the measured time-of-flight signals clearly indicates the increase in the spectra (1 to 10 MeV) from the breakup of deuterium in the reaction vessel. The excited states of (a) oxygen (7.0 MeV) and (b) carbon (4.44, 7.65, 9.64 MeV) are observed in the time-of-flight spectra.

is seen in spectra from the H_2O and D_2O vessels in addition to several excited states (4.44, 7.65, 9.64 MeV) observed in the spectra from the C_6H_6 and C_6D_6 vessels. An additional test included a vessel filled with a 50/50 mixture of H_2O and D_2O to verify the expected decrease in the neutron signal (see Fig. 153.8) from the breakup caused by the reduction of the deuterium concentration in the compound mixture.

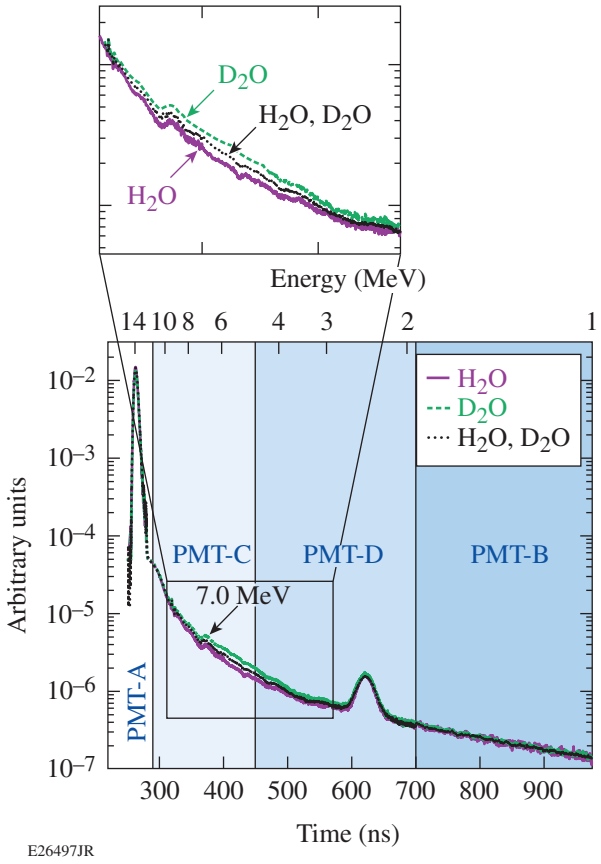

Figure 153.8
Three different vessels filled with water (H_2O), heavy water (D_2O), and an equimolar mixture of water and heavy water were used to measure the nTOF spectrum. A change in the neutron-induced breakup is evident from the vessel filled with the equimolar concentration of H_2O and D_2O.

To extract the deuteron breakup contribution, the signal from the vessel containing the non-deuterated compounds was subtracted from the signal generated from the vessels that retained the deuterated compounds. This approach is advantageous since it removes the contributions from the inelastic scattering of both carbon and oxygen along with any additional scattering and nonlinear scintillator effects that arise from the experimental configuration.

2. Yield Calculation

The residual signal from the subtraction is assumed to be entirely a result of the neutron-induced breakup reaction. To calculate the breakup neutron yield from the measured signal, the experimental neutron yield as a function of energy spectrum is inferred using Eq. (6) as

$$\mathrm{d}Y_{\mathrm{n,2n}}(t_{\mathrm{n}}) = \frac{k_1}{k_2}\frac{1}{\chi_{\mathrm{n}}(E_{\mathrm{n}})E_{\mathrm{n}}^{\alpha}} I(t_{\mathrm{n}})\mathrm{d}t_{\mathrm{n}}, \tag{10}$$

where k_1/k_2 is the constant determined from the calibration with D_2 neutrons. The yields for the campaign with the deuterated water and benzene are weighted according to the number of shots on each vessel as measured by the diagnostic for the two separate campaigns. Both campaigns have been restricted to measuring the neutron contribution at or below 10.5 MeV. The neutron spectrum above this energy is dominated by the intense primary D–T yield, obscuring the breakup neutron component. In this experimental setup, the region from 2 MeV to 3 MeV is excluded since the D_2 peak contribution can vary because of the thermal broadening from the fusing plasma.[32]

3. Error Analysis

The error within the $Y_{\mathrm{n,2n}}$ yield measurement can be separated into three categories: statistical error, systematic error, and other uncertainties. The number of neutrons measured in the 13.4-m spectrometer is in the range between 10^4 and 10^5, which leads to a statistical uncertainty of ~1%. Systematic uncertainties are associated with a number of steps involved when calibrating the detector. A significant contribution to uncertainty in the yield measurement arises from the Y_{D_2} yield reference used to calibrate the nTOF spectrometer. A direct *in-situ* calibration method using CR-39 range filter proton detectors has been successfully employed by measuring D–D neutron and proton yields from a series of exploding-pusher implosions on OMEGA.[33] The present D–D yield uncertainty used to cross-calibrate the diagnostic to calculate the cross section is 9%. Upcoming experiments will be performed to further reduce this uncertainty. Another very sensitive detector effect originates from the nonlinear light output of the scintillator required to infer the neutron yield over a broad energy range. For most organic scintillators, the light output is nonlinear for proton recoil energies below 5 MeV, while becoming approximately linear at higher energies. Calculating the yield using the different measured light sensitivities discussed in the literature for the scintillating compound used in this experiment gives a 2% uncertainty.

Inaccuracies in the detection method include signal distortion from the photomultiplier tube, transmission cable, and the recording device. A systematic uncertainty must be taken into consideration when the signals are subtracted from one another. This includes the signal-to-background and the standard deviation in the digitized signal after performing the subtraction. To investigate and qualify the systematic effects from the PMT and cable, offline testing was used to fully characterize the detection system and determine the optimal operating range to ensure signal linearity to within 1%. To quantify the additional scattering contributed from the vessel, two different implosions were performed: one with an empty vessel and one with the vessel and support hardware completely removed from the line of sight. The results show that the introduction of the reaction vessel produced an insignificant amount (<1%) of additional scattering. The inferred yield from the breakup of deuterium with the aforementioned errors added in quadrature as a function of energy is given in Table 153.II.

Table 153.II: The number of breakup neutrons as a function of energy from C_6D_6 and D_2O.

Energy (MeV)	$Y_{n,2n}$ (C_6D_6) $Y_{DT} = 7.20 \times 10^{13}$	$Y_{n,2n}$ (D_2O) $Y_{DT} = 5.79 \times 10^{13}$
0.5 to 1.0	$2.94 \times 10^4 \pm 7.29 \times 10^4$	N/A
1.0 to 1.5	$3.75 \times 10^4 \pm 3.29 \times 10^4$	$1.32 \times 10^4 \pm 4.87 \times 10^4$
1.5 to 2.0	$1.58 \times 10^4 \pm 1.89 \times 10^4$	$1.98 \times 10^4 \pm 2.75 \times 10^4$
3.0 to 3.5	$5.73 \times 10^4 \pm 9.64 \times 10^3$	$6.74 \times 10^4 \pm 2.09 \times 10^4$
3.5 to 4.0	$6.86 \times 10^4 \pm 2.13 \times 10^4$	$8.07 \times 10^4 \pm 2.61 \times 10^4$
4.0 to 4.5	$1.06 \times 10^5 \pm 1.93 \times 10^4$	$1.29 \times 10^5 \pm 2.50 \times 10^4$
4.5 to 5.0	$1.45 \times 10^5 \pm 1.89 \times 10^4$	$1.66 \times 10^5 \pm 2.79 \times 10^4$
5.0 to 5.5	$1.69 \times 10^5 \pm 2.11 \times 10^4$	$1.98 \times 10^5 \pm 2.65 \times 10^4$
5.5 to 6.0	$1.65 \times 10^5 \pm 1.71 \times 10^4$	$2.00 \times 10^5 \pm 2.59 \times 10^4$
6.0 to 6.5	$1.47 \times 10^5 \pm 1.99 \times 10^4$	$1.81 \times 10^5 \pm 2.48 \times 10^4$
6.5 to 7.0	$1.37 \times 10^5 \pm 1.61 \times 10^4$	$1.83 \times 10^5 \pm 2.74 \times 10^4$
7.0 to 7.5	$1.14 \times 10^5 \pm 1.88 \times 10^4$	$1.53 \times 10^5 \pm 2.04 \times 10^4$
7.5 to 8.0	$9.06 \times 10^4 \pm 1.55 \times 10^4$	$1.47 \times 10^5 \pm 1.80 \times 10^4$
8.0 to 8.5	$9.12 \times 10^4 \pm 1.23 \times 10^4$	$1.42 \times 10^5 \pm 1.50 \times 10^4$
8.5 to 9.0	$8.10 \times 10^4 \pm 1.71 \times 10^4$	$1.20 \times 10^5 \pm 1.60 \times 10^4$
9.0 to 9.5	$5.18 \times 10^4 \pm 6.57 \times 10^4$	$1.06 \times 10^5 \pm 3.71 \times 10^4$
9.5 to 10.0	$6.28 \times 10^4 \pm 1.90 \times 10^4$	$1.14 \times 10^5 \pm 1.42 \times 10^4$
10.0 to 10.5	$6.29 \times 10^4 \pm 3.99 \times 10^4$	$9.46 \times 10^4 \pm 4.77 \times 10^4$
10.5 to 11.0	N/A	$6.41 \times 10^4 \pm 1.20 \times 10^4$

The energy resolution is obtained from the arrival time of the neutrons, which has been absolutely calibrated from the hardware timing fiducial. Lower-energy neutrons span a larger time window with a larger number of digitized bins on the oscilloscope, resulting in a lower uncertainty in the energy resolution (~2 keV). Higher-energy neutrons have an increasingly smaller arrival time window, which reduces the number of bins and leads to a larger uncertainty (~150 keV) in the energy resolution.

4. Angle-Averaged Double-Differential Cross Section

With the yields from the neutron-induced breakup reaction, the double-differential cross section as a function of energy is calculated using the following relation:

$$Y_{n,2n} = m_n \eta_D \int_0^{I_{NRV}} \int_0^{\Omega_{dia}(x_{NRV})} Y_{inc}(x_{NRV}) \times \int_0^{E_{max}} [\cos(\theta)] \frac{d^2\sigma_{n,2n}}{d\Omega dE} \tau_{NRV}(E, x_{NRV}) \times \varepsilon_{dia}(E) dE d\Omega dx_{NRV},$$

where

- $Y_{n,2n}$ = the number of detected neutrons from the neutron-induced breakup reaction,
- m_n = the multiplicity for the number of generated neutrons from the breakup ($m_n = 2$),
- η_D = the number density of deuterium in the reaction vessel,
- l_{NRV} = the length of the reaction vessel,
- Ω_{dia} (x_{NRV}) = the solid angle of the detector at x_{NRV},
- Y_{inc} (x_{NRV}) = the number of incident 14.03-MeV neutrons at x_{NRV},
- E_{max} [cos (θ)] = the maximum neutron energy versus laboratory angle θ,
- $d^2\sigma_{n,2n}/d\Omega dE$ = the double-differential cross section for the neutron-induced breakup reaction,
- $\tau_{NRV}(E, x_{NRV})$ = the transmission of neutron with energy E through the reaction vessel at x_{NRV}, and

- $\varepsilon_{dia}(E)$ = the fraction of neutrons at energy E interacting inside detector.

In the geometry of the experimental setup (see Fig. 153.1), the accepted angle of the breakup neutrons from the reaction vessel to the diagnostic is in the range of 3.5°±3.5°. The angle-averaged $\left\langle d^2\sigma / dE_n d\Omega_n \right\rangle_{NRV}$ double-differential cross section inferred from the time-of-flight measurements using the D_2O and C_6D_6 vessel is shown in Fig. 153.9. The inferred double-differential cross section has been compared with the available experimental data, and recent theoretical calculations are shown in Fig. 153.10. A complete list of the experimental parameters is given in Table 153.III.

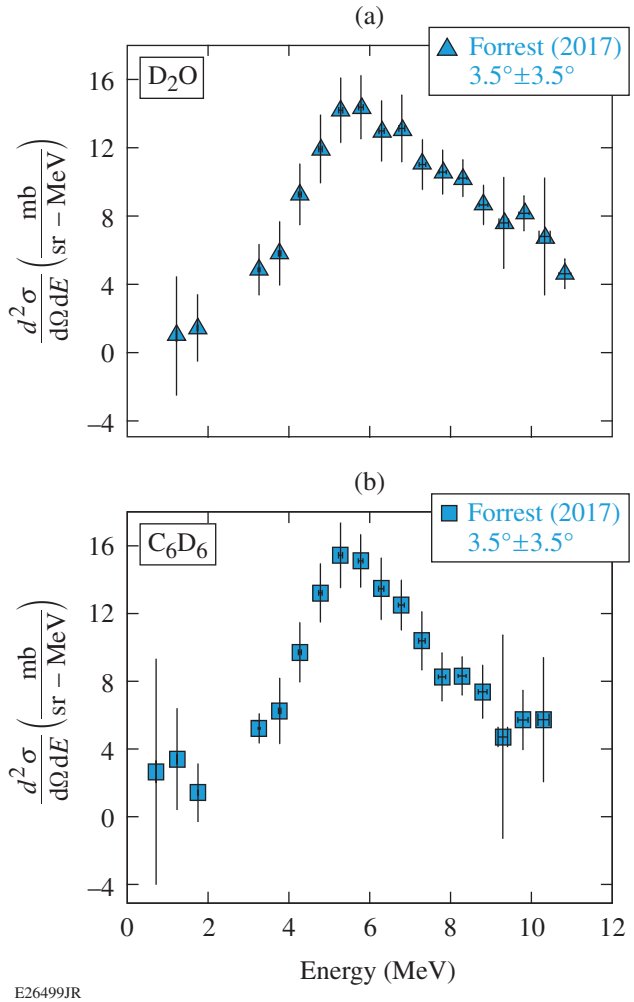

Figure 153.9
(a) The angle-averaged double-differential cross section (triangles) is calculated from the measured neutron yield as a function of energy using the heavy water (D_2O) NRV as the source for the breakup reaction. (b) The angle-averaged (in the range of 3.5°±3.5°) double-differential cross section (squares) is compared to earlier measurements obtained at an angle of 10° (Ref. 34).

5. Multiple Scattering Effects

Scattering of the neutrons generated from the breakup reaction in the vessel could affect the inferred cross section calculated from the neutron yield measured by the diagnostic. The neutron transport code MCNP was used to model the

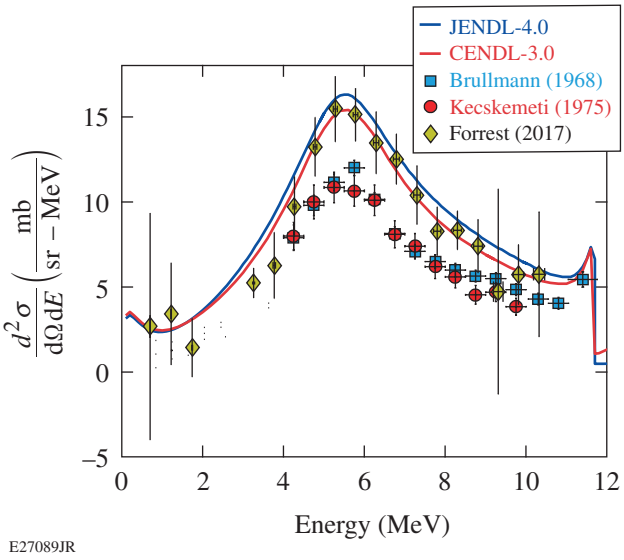

Figure 153.10
Neutron spectra $d^2\sigma/(d\Omega dE)$ of the reaction $2H(n,2n)p$ at a primary neutron energy of 14 MeV. The inferred double-differential cross section from OMEGA has been compared with available experimental data and recent theoretical calculations.

Table 153.III: The geometric parameters for the experimental setup.

Equipment	Parameter	in cm
Nuclear reaction vessel (NRV)	$d_{face\ NRV}$	8.80
	x_{NRV}	$x_{NRV} = 0 < x_{NRV} < l_{NRV}$
	l_{NRV}	7.501
	$r_{face\ NRV}$	0.483
	$r_{rearA\ NRV}$	2.169
	$r_{rearB\ NRV}$	1.676
	$l_{cone\ NRV}$	5.885
	$l_{rearA\ NRV}$	7.145
Mid-beam collimator (MBC)	d_{face}	737.2
	r_{MBC}	5.588
	l_{MBC}	71.12
13.4-m neutron time of flight (nTOF)	d_{face}	1340
	x_{dia}	$0 < x_{dia} < l_{dia}$
	l_{dia}	10.16
	r_{dia}	10.16

experimental setup.[24] The simulations included a high-yield neutron source incident on a nuclear reaction vessel and an infinitely thin plane (surface of the diagnostic) positioned 13.4 m away. A special tally program was written that extracted only the neutrons that were born from the neutron-induced breakup and crossed the surface of the detector plane. This tally recorded the location of the last scatter event in the vessel, the number of scatter events in the vessel, the type of scatter event it underwent (i.e., elastic, inelastic, etc.), and which element had an event. This information was used to interpret the addition of multiple scattering of the neutrons as they exited the vessel and crossed the surface of the diagnostic. These simulations show that the energy spectrum is affected only at energies below 1 MeV (<3%).

Summary and Discussion

In summary, high-quality data have been recorded using an ICF platform to induce the breakup reaction of deuterium and infer the angle-averaged double-differential cross section. The experiment measured the energy spectrum of the deuterium breakup reaction from 0.5 MeV to 10.5 MeV averaged over an angular region from $\theta_{lab} = 3.5° \pm 3.5°$. A statistical uncertainty of ~1% is inferred with a systematic uncertainty of ~10% for the measured neutron yield used to calculate the cross section for the induced breakup of deuterium. This cross section has been compared to earlier experimental measurements for an accelerator-based platform. This experiment highlights that the OMEGA Laser System provides a unique platform on which to study neutron-induced reactions with a high signal-to-background ratio in a single campaign.

Future experiments will focus on upgrading our diagnostics to resolve the final-state interaction peak at 11.8 MeV. These improvements include higher-bit analog-to-digital converter oscilloscopes and faster gate units with less than 2-ns recovery times.

Additional reaction vessels have been constructed that contain other light-Z elements such as ^{7}Li and ^{9}Be to measure the (n,2n) reactions. There is sparse data for ^{7}Li with large differences in the published measurements. Recent experiments on OMEGA have measured the inelastic scattering of 14-MeV neutrons from ^{7}Li. Initial measurements indicate a measurable neutron energy spectrum. Detailed analysis is underway to infer the neutron-induced breakup reaction from the experimental data. A larger measurement database exists for ^{9}Be, and it would be useful to compare data from an implosion neutron source with an accelerator neutron source.

ACKNOWLEDGMENT

This material is based upon work supported by the Department of Energy National Nuclear Security Administration under Award Number DE-NA0001944, the University of Rochester, and the New York State Energy Research and Development Authority.

REFERENCES

1. C. D. Zhou and R. Betti, Phys. Plasmas **15**, 102707 (2008); **16**, 079905(E) (2009).
2. T. R. Boehly, D. L. Brown, R. S. Craxton, R. L. Keck, J. P. Knauer, J. H. Kelly, T. J. Kessler, S. A. Kumpan, S. J. Loucks, S. A. Letzring, F. J. Marshall, R. L. McCrory, S. F. B. Morse, W. Seka, J. M. Soures, and C. P. Verdon, Opt. Commun. **133**, 495 (1997).
3. J. Nuckolls *et al*., Nature **239**, 139 (1972).
4. S. Atzeni and J. Meyer-ter-Vehn, *The Physics of Inertial Fusion: Beam Plasma Interaction, Hydrodynamics, Hot Dense Matter*, 1st ed., International Series of Monographs on Physics, Vol. 125 (Oxford University Press, Oxford, 2004).
5. G. S. Fraley and R. J. Mason, Phys. Rev. Lett. **35**, 520 (1975).
6. J. M. Soures, R. L. McCrory, C. P. Verdon, A. Babushkin, R. E. Bahr, T. R. Boehly, R. Boni, D. K. Bradley, D. L. Brown, R. S. Craxton, J. A. Delettrez, W. R. Donaldson, R. Epstein, P. A. Jaanimagi, S. D. Jacobs, K. Kearney, R. L. Keck, J. H. Kelly, T. J. Kessler, R. L. Kremens, J. P. Knauer, S. A. Kumpan, S. A. Letzring, D. J. Lonobile, S. J. Loucks, L D. Lund, F. J. Marshall, P. W. McKenty, D. D. Meyerhofer, S. F. B. Morse, A. Okishev, S. Papernov, G. Pien, W. Seka, R. Short, M. J. Shoup III, M. Skeldon, S. Skupsky, A. W. Schmid, D. J. Smith, S. Swales, M. Wittman, and B. Yaakobi, Phys. Plasmas **3**, 2108 (1996).
7. J.-M. Laborie *et al*., Eur. Phys. J. A **48**, 87 (2012).
8. J. S. C. McKee, Rep. Prog. Phys. **33**, 691 (1970).
9. C. J. Forrest, V. Yu. Glebov, V. N. Goncharov, J. P. Knauer, P. B. Radha, S. P. Regan, M. H. Romanofsky, T. C. Sangster, M. J. Shoup, and C. Stoeckl, Rev. Sci. Instrum. **87**, 11D814 (2016).
10. J. H. Nuckolls, Lawrence Livermore National Laboratory, Livermore, CA, Report UCRL-ID-131075 (1988).
11. E. B. Goldman, J. A. Delettrez, and E. I. Thorsos, Nucl. Fusion **19**, 555 (1979).
12. J. Nuckolls, J. Emmett, and L. Wood, Phys. Today **26**, 46 (1973).
13. C. Stoeckl, R. Boni, F. Ehrne, C. J. Forrest, V. Yu. Glebov, J. Katz, D. J. Lonobile, J. Magoon, S. P. Regan, M. J. Shoup III, A. Sorce, C. Sorce, T. C. Sangster, and D. Weiner, Rev. Sci. Instrum. **87**, 053501 (2016).
14. C. J. Forrest, P. B. Radha, V. Yu. Glebov, V. N. Goncharov, J. P. Knauer, A. Pruyne, M. Romanofsky, T. C. Sangster, M. J. Shoup III, C. Stoeckl, D. T. Casey, M. Gatu-Johnson, and S. Gardner, Rev. Sci. Instrum. **83**, 10D919 (2012).
15. C. Stoeckl, M. Cruz, V. Yu. Glebov, J. P. Knauer, R. Lauck, K. Marshall, C. Mileham, T. C. Sangster, and W. Theobald, Rev. Sci. Instrum. **81**, 10D302 (2010).

16. R. Lauck *et al*., IEEE Trans. Nucl. Sci. **56**, 989 (2009).

17. Photek Ltd., St. Leonards on Sea, East Sussex, TN38 9NS, United Kingdom.

18. DG645 Digital Delay Generator, Stanford Research Systems Inc., Sunnyvale, CA 94089-2279.

19. Pasternack, Irvine, CA, 92614-6002.

20. Tektronix Inc., Beaverton, OR 97077.

21. Teledyne Isco, Lincoln, NE 68504-1328.

22. BroadWave Technologies, Greenwood, IN, 46143-1443.

23. Keysight Technologies Inc., Santa Rosa, CA 95403-1738.

24. X-5 Monte Carlo Team, Los Alamos National Laboratory, Los Alamos, NM, Report LA-UR-03-1987 (2008).

25. M. B. Chadwick *et al*., Nucl. Data Sheets **107**, 2931 (2006).

26. G. F. Knoll, *Radiation Detection and Measurement*, 3rd ed. (Wiley, New York, 2000).

27. B. von Krosigk *et al*., Eur. Phys. J. C **73**, 2390 (2013).

28. R. L. Craun and D. L. Smith, Nucl. Instrum. Methods **80**, 239 (1970).

29. V. V. Verbinski *et al*., Nucl. Instrum. Methods **65**, 8 (1968).

30. V. Yu. Glebov, T. C. Sangster, C. Stoeckl, J. P. Knauer, W. Theobald, K. L. Marshall, M. J. Shoup III, T. Buczek, M. Cruz, T. Duffy, M. Romanofsky, M. Fox, A. Pruyne, M. J. Moran, R. A. Lerche, J. McNaney, J. D. Kilkenny, M. J. Eckart, D. Schneider, D. Munro, W. Stoeffl, R. Zacharias, J. J. Haslam, T. Clancy, M. Yeoman, D. Warwas, C. J. Horsfield, J.-L. Bourgade, O. Landoas, L. Disdier, G. A. Chandler, and R. J. Leeper, Rev. Sci. Instrum. **81**, 10D325 (2010).

31. O. Landoas, V. Yu. Glebov, B. Rossé, M. Briat, L. Disdier, T. C. Sangster, T. Duffy, J. G. Marmouget, C. Varignon, X. Ledoux, T. Caillaud, I. Thfoin, and J.-L. Bourgade, Rev. Sci. Instrum. **82**, 073501 (2011).

32. H. Brysk, Plasma Phys. **15**, 611 (1973).

33. C. J. Waugh, M. J. Rosenberg, A. B. Zylstra, J. A. Frenje, F. H. Séguin, R. D. Petrasso, V. Yu. Glebov, T. C. Sangster, and C. Stoeckl, Rev. Sci. Instrum. **86**, 053506 (2015).

34. M. Brullmann *et al*., Nucl. Phys. A **117**, 419 (1968)